nature communications

Article

https://doi.org/10.1038/s41467-025-58141-6

Dipeptidyl peptidase DPF-3 is a gatekeeper of microRNA Argonaute compensation in animals

Received: 6 September 2024

Accepted: 13 March 2025

Louis-Mathieu Harvey[1,2], **Pierre-Marc Frédérick**[1,2,8], **Rajani Kanth Gudipati**[3,8], **Pascale Michaud**[1,2], **François Houle**[1,2], **Daniel Young**[4,5], **Catherine Desbiens**[1,2], **Shanna Ladouceur**[1,2], **Antoine Dufour**[4,5], **Helge Großhans**[6,7] & **Martin J. Simard**[1,2] ✉

MicroRNAs (miRNAs) are essential regulators involved in multiple biological processes. To achieve their gene repression function, they are loaded in miRNA-specific Argonautes to form the miRNA-induced silencing complex (miRISC). Mammals and *C. elegans* possess more than one paralog of miRNA-specific Argonautes, but the dynamic between them remains unclear. Here, we report the conserved dipeptidyl peptidase DPF-3 as an interactor of the miRNA-specific Argonaute ALG-1 in *C. elegans*. Knockout of *dpf-3* increases ALG-2 levels and miRISC formation in *alg-1* loss-of-function animals, thereby compensating for ALG-1 loss and rescuing miRNA-related defects observed. DPF-3 can cleave an ALG-2 N-terminal peptide in vitro but does not appear to rely on this catalytic activity to regulate ALG-2 in vivo. This study uncovers the importance of DPF-3 in the miRNA pathway and provides insights into how multiple miRNA Argonautes contribute to achieving proper miRNA-mediated gene regulation in animals.

MicroRNAs (miRNAs) form a class of endogenous small non-coding RNAs that can regulate gene expression at the post-transcriptional level. These molecules play a major role across almost all living organisms as they can regulate a plethora of biological processes during development and aging[1]. To achieve their function, miRNAs must be loaded into an Argonaute protein to form an active complex named miRNA-induced silencing complex (miRISC). This complex may include other factors such as the deadenylation and decapping machinery through its interaction with a GW182 scaffold protein, one of the main miRNA-specific Argonaute interactors[2–4]. The miRNA guides miRISC to its target mRNAs, usually exploiting base-pairing to regions of incomplete complementarity in the mRNA 3′-untranslated region (UTR)[5]. Upon binding to the mRNA, the miRISC can silence its translation by either inhibiting translation, degrading the mRNA, or both[6,7]. While the outcome of the miRISC binding to its mRNA target is post-translational repression, it is not well understood what determines which silencing mechanism is employed. It has been suggested that the mRNA's fate after being targeted is dependent on the context[8–11]. Therefore, the miRISC composition and preferred repression mechanism can vary between cell types and stages of the development of the organism[6].

The Argonaute superfamily of proteins is divided into three main paralogous groups: Argonaute-like proteins (AGO), PIWI-like proteins (PIWI) and worm-specific proteins (WAGO)[12]. Those proteins have a bi-lobed architecture organized in four distinct main domains (N, PAZ, MID and PIWI) supported with two linker domains (L1 and L2)[13],

---

[1]Oncology Division, CHU de Québec – Université Laval Research Center, Québec, Canada. [2]Université Laval Cancer Research Centre, Québec, Canada. [3]Centre for Advanced Technologies, Adam Mickiewicz University, Poznań, Poland. [4]Department of Physiology & Pharmacology, University of Calgary, Calgary, Canada. [5]Department of Biochemistry & Molecular Biology, University of Calgary, Calgary, Canada. [6]Friedrich Miescher Institute for Biomedical Research, Basel, Switzerland. [7]University of Basel, Basel, Switzerland. [8]These authors contributed equally: Pierre-Marc Frédérick, Rajani Kanth Gudipati. ✉e-mail: martin.simard@crchudequebec.ulaval.ca

conserved in all different Argonaute groups across several species[14,15]. In *C. elegans*, the highly similar ALG-1 and ALG-2 constitute the two main miRNA-specific Argonautes. Structurally, they mainly differ by their N-terminal domain, which is extended in ALG-1 compared to ALG-2[16]. They are both expressed in all tissues with the noticeable exception of the pharynx, and the germline and a subset of head neurons, where ALG-1 and ALG-2 are exclusively expressed, respectively[16,17]. Because of their similarities, their function is thought to be mostly redundant. This is highlighted by the fact that animals expressing only one of these Argonautes are viable, but the loss of both is lethal[18,19]. However, there are some differences in their expression pattern during development and aging[20]. Indeed, ALG-2 is dominantly present during embryogenesis, while ALG-1 rises when approaching the larval stages and stays high before falling off at the adult stage. Also, both Argonautes bind to a high proportion of identical miRNAs, but some are specific to one or the other[20]. This illustrates that both miRNA-specific Argonautes have exclusive functionality depending on the cellular and developmental context.

Like *C. elegans*, mammals also possess more than one miRNA-specific Argonaute. They have four different Argonaute proteins that can act in the miRNA pathway, namely AGO1-4. Those Argonautes also have high sequence identity between them (~80%), with most of their differences residing within their N domains, and they also share expression in most tissues[21]. Most miRNAs are associated with all four miRNA-specific Argonautes[22], raising the question of whether they work redundantly. Recent studies described the unique roles of individual AGOs[23–26] along with differences in their respective structure[27]. Those data highlight that akin to *C. elegans*, mammalian AGOs can assume different specific functions depending on the cellular and developmental context despite their similarities. However, the relevant regulatory mechanisms influencing miRNA-specific Argonautes' functions in species with multiple paralogs remain poorly understood.

In this study, we aimed to address what can drive miRNA-specific Argonautes to function differently by discovering new regulators using *C. elegans* as a model system. We used genetic and molecular approaches to characterize dipeptidyl peptidase DPF-3 as an interacting partner of miRNA-specific Argonautes. We demonstrate that *dpf-3* physically and genetically interacts with the miRNA pathway, and that its knockout suppresses *alg-1* loss-of-function defects both at the phenotypical and molecular level. We also show that DPF-3 regulates ALG-2 protein level and its ability to compensate for miRNA function in the absence of its paralog ALG-1.

Results

Dpf-3 is a physical and genetic interactor of ALG-1

We first set out to discover new interactors of the miRISC by performing an ALG-1 immunoprecipitation followed by mass spectrometry (IP-MS) analysis using a CRISPR-Cas9 engineered strain expressing a FLAG-HA tag at *alg-1* endogenous loci. With this method, we readily identified AIN-1 and AIN-2, orthologs of TNRC6/GW182 and known interacting partners of ALG-1[10,28,29] (Fig. 1a). Additionally, we consistently observed strong enrichment of DPF-3 (Fig. 1a), not previously known to function in the miRNA pathway. We also performed this experiment with samples treated with either RNase inhibitors or RNase and found an enrichment for DPF-3 in both conditions (Supplementary Fig. 1a, b). DPF-3 is a member of the dipeptidyl peptidase 4 (DPP4) serine protease family and is the *C. elegans* ortholog of mammalian DPP8/9, which play important roles in immunity, inflammation, and tumor biology, among others[30]. Members of this protease family are exopeptidases that cleave dipeptides off the N-terminus from their substrates, with a preference for cleaving after proline or alanine when in second position[31–33]. Recently, DPF-3 was shown to regulate the endogenous siRNA pathway by mediating the processing of *C. elegans*-specific Argonautes WAGO-1 and WAGO-3[34]. This raised the question of whether this dipeptidyl peptidase-mediated regulatory mechanism could also be extended to Argonautes of a conserved pathway, such as miRNA-mediated gene regulation.

To explore a potential function of *dpf-3* in the regulation of the miRNA pathway, we crossed the *dpf-3(xe68)* null strain[34] into the *alg-1(gk214)* loss-of-function strain. We investigated the effect of *dpf-3(xe68)* on *alg-1(gk214)* phenotypes associated with dysfunction of the miRNA pathway. We first monitored the number of hypodermal cells named seam cells, which arise from asymmetric division during the animal larval development, resulting in sixteen lateral seam cells distributed on each side of the animal[35]. Given that their proliferation and terminal differentiation are tightly regulated by miRNAs[18], in events where the miRNA pathway is defective, such as in *alg-1* loss-of-function mutants, the number of seam cells can be greater than sixteen[36,37]. Using a strain expressing GFP under seam cell-specific promoter, we observed that the seam cell number in most *alg-1(gk214)* animals is greater than sixteen, as expected (Fig. 1b and Supplementary Fig. 1c). While the *dpf-3(xe68)* mutation alone has no effect on the seam cell proliferation, its loss in *alg-1(gk214)* animals significantly decreases the seam cell number to an amount comparable to WT animals. We next verified the presence of defects in the formation of the cuticular structure named alae, which is formed after seam cells division and fusion during the transition to adulthood[38]. Over 20% of *alg-1(gk214)* animals showed a gap in the alae structure compared to no defect in the WT and *dpf-3(xe68)* worms (Fig. 1c). The double mutant also displayed no alae gap, demonstrating rescue of the *alg-1(gk214)*-related phenotype by the loss of *dpf-3* as seen in the seam cells count. Another phenotype we scored is the vulval bursting happening at the larva-to-adulthood transition, known to occur at restrictive temperatures in *alg-1(gk214)* animals. This type of lethality is associated with the misregulation of the let-7 miRNA target LIN-41 mRNA, an important heterochronic gene essential for controlling the proper development of the vulva at the larva-to-adult transition in *C. elegans*[39]. WT and *dpf-3(xe68)* worms had no bursting at 25 °C whereas over 10% of *alg-1(gk214)* animals died from bursting after reaching adulthood (Fig. 1d). While some bursting was still observable in *dpf-3(xe68);alg-1(gk214)* animals (~2%), we observed a significant decrease in the number of worms bursting, showing the *dpf-3(xe68)* mutation can also rescue this *alg-1(gk214)* related phenotype. We next investigated whether functional miRNAs are required for the suppression of the observed phenotypes. We used a strain carrying a let-7 miRNA mutation that leads to defective regulation of the LIN-41 mRNA in a temperature-sensitive manner (*let-7(n2853)* allele). None of the WT and *dpf-3(xe68)* animals died by bursting, while *let-7(n2853)* and *dpf-3(xe68);let-7(n2853)* worms had similar bursting rate (Supplementary Fig. 1d). This suggests that functional miRNAs are required to achieve phenotype rescue, at least for let-7 specific phenotypes. Overall, we conclude from this data that *dpf-3* is a physical and genetic interactor of miRNA-specific Argonaute ALG-1.

Dpf-3 depletion restores normal miRNA repression in *alg-1* loss-of-function animals

Next, we wondered if our observed rescue would extend to the molecular level. It is well established that *alg-1* loss-of-function greatly affects the animal's capacity to maintain post-transcriptional gene regulation by the miRNA pathway, in part due to diminished miRNA production or stability[20,40]. Therefore, we first verified the effect of the loss of *dpf-3* in *alg-1(gk214)* animals on miRNA steady-state by small RNA sequencing and compared the data to WT, *dpf-3(xe68),* and *alg-1(gk214)* animals. Since most of the phenotypes we observed previously (Fig. 1) appear at the larva-to-adult transition, we monitored the miRNA levels in replicates of young adult worm populations. We performed Principal Component Analysis (PCA) and found that the three independent populations of their respective genotype cluster well among themselves (Supplementary Fig. 2), indicating low variance between the replicates. As expected, *alg-1(gk214)* animals had the most effect on miRNA levels as 75 out of 166 (45.2%) were either increased or decreased by at least two-fold compared to WT animals (Fig. 2a). By contrast, *dpf-3(xe68);alg-1(gk214)* animals had fewer miRNAs misregulated (20 out of 166, or 12.1%) and had a miRNA expression pattern similar to WT and *dpf-3(xe68)* animals (Fig. 2a and Supplementary

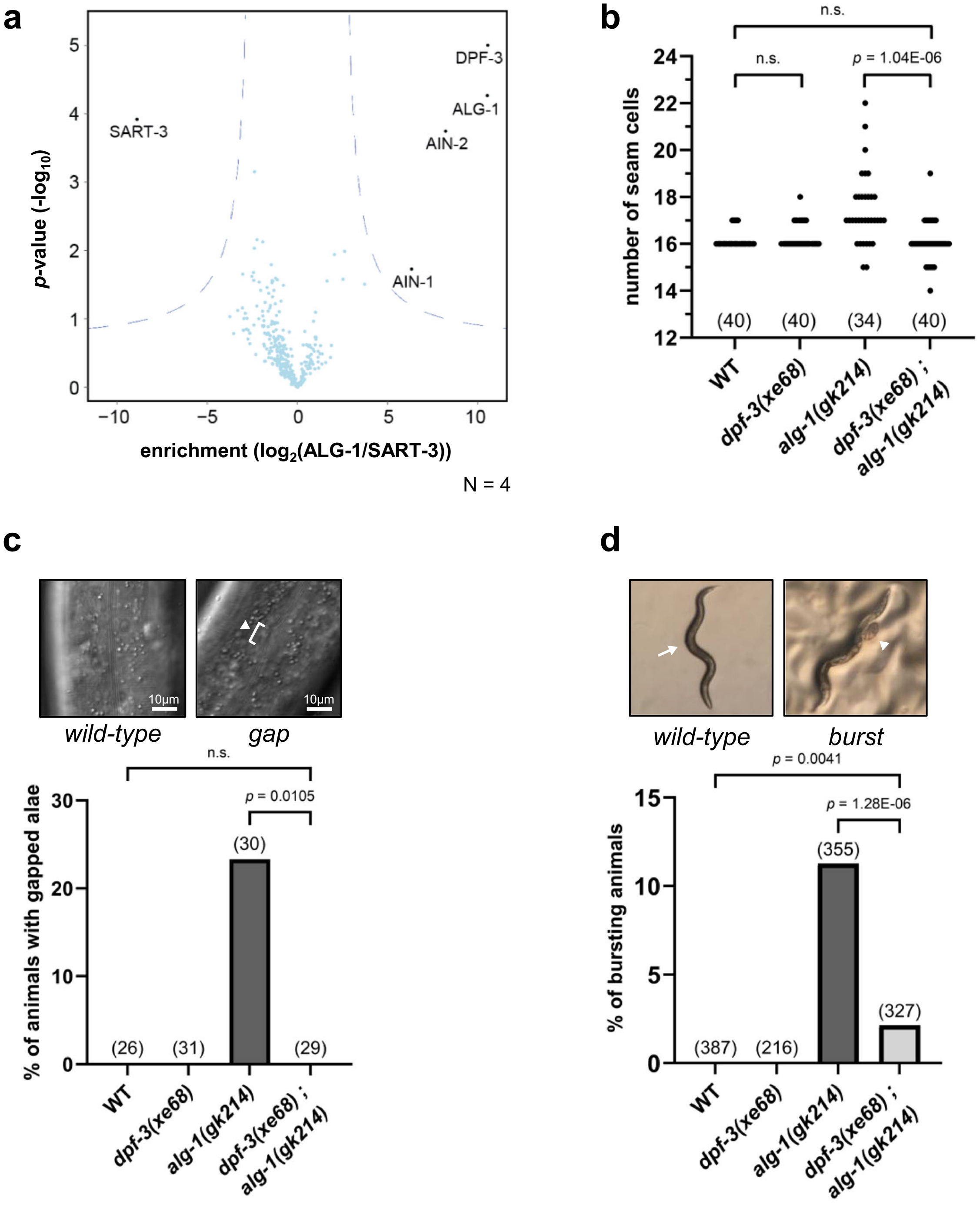

Fig. 1 | *Dpf-3* physically and genetically interacts with the miRNA pathway. a IP-MS of ALG-1. The x-axis indicates the fold enrichment of the bait proteins and their interacting partners over control (SART-3). Each dot represents a distinct interacting partner. Specific and significant interacting partners are shown. False Discovery Rate (FDR) of 0.05 was used. Exact *p*-values were calculated by two-tailed Student *t*-test and are indicated for each interactor on the Y-axis of the volcano plot. *N* = 4. **b** Seam cell number in adult WT, *dpf-3(xe68)*, *alg-1(gk214)* and *dpf-3(xe68);alg-1(gk214)* worms. Each dot represents a single animal. The number in parenthesis represents the number of animals scored for each genotype. *P*-value was calculated by two-tailed Mann-Whitney test. n.s. = non-significant. **c** Top: DIC pictures showing an example of normal alae structure and gapped alae structure (white arrowhead points to the gap in the structure and the bracket shows the length of the gap). Bottom: Percentage of WT, *dpf-3(xe68)*, *alg-1(gk214)* and *dpf-3(xe68);alg-1(gk214)* worms displaying an alae gap phenotype at 20 °C. The number in parenthesis represents the number of animals scored for each genotype. *P*-values were calculated by two-sided Fisher's exact test. n.s. = non-significant. **d** Percentage of WT, *dpf-3(xe68)*, *alg-1(gk214)* and *dpf-3(xe68);alg-1(gk214)* worms displaying the bursting through the vulva phenotype at 25 °C. Number in parenthesis represents the number of worms scored. Pictures show an example of a normally developed worm versus a burst worm, where the white arrow points at a normal vulva and the white arrowhead points at the gonad sticking out of the vulva. *P*-values were calculated by two-sided Fisher's exact test.

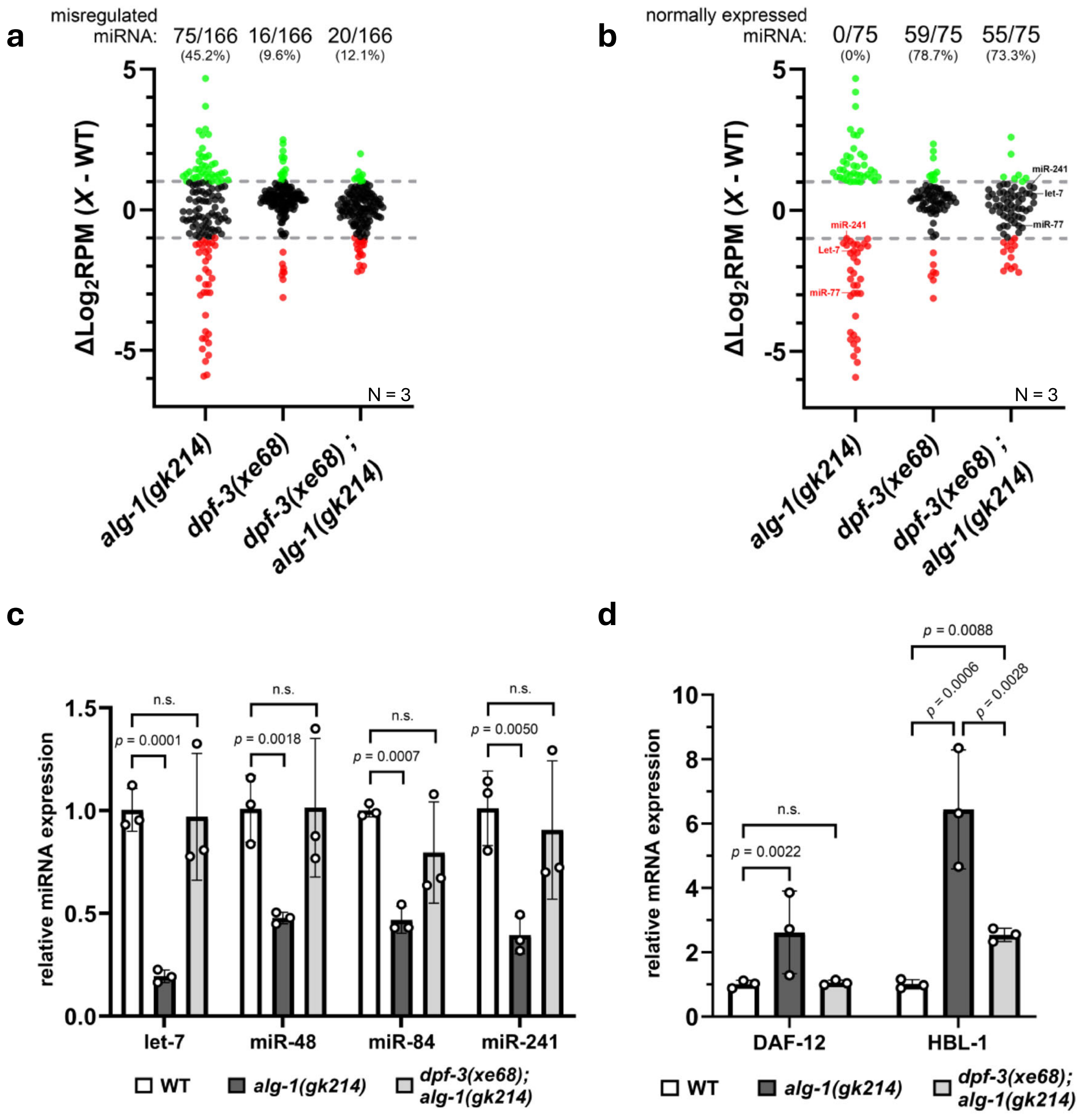

Fig. 2 | Removal of *dpf-3* in *alg-1* loss-of-function animals restores normal miRNA regulation of transcripts. a ΔLog_2 of RPM of miRNA sequencing data where the WT values are subtracted from the *dpf-3(xe68), alg-1(gk214)* and *dpf-3(xe68);alg-1(gk214)* values. Each dot represents a single miRNA, where green dots are miRNAs more expressed than WT and red dots are miRNAs less expressed than WT. Black dots represent miRNAs that are within normal expression thresholds (gray dashed lines). The proportion of miRNAs misregulated by at least ±1 ΔLog_2 appear on top of each condition. Each dot is a mean of 3 biological replicates normalized on the total reads. **b** ΔLog_2 of RPM of miRNA sequencing data where only miRNAs that were up- or downregulated in *alg-1(gk214)* animals were selected and quantified in specified genetic backgrounds. The proportion of those miRNAs that are within normal expression thresholds (gray dashed lines) appear on top of each condition. **c**, **d** RT-qPCR was performed on total RNA extracts of WT, *alg-1(gk214)* and *dpf-3(xe68);alg-1(gk214)* worms to measure the relative expression of the let-7 miRNA family members and their targets. Data are presented as mean values of three biological replicates (white dots) ± SD. MiRNA levels were normalized using sn2841, and miRNA target levels were normalized using *tba-1*. *P*-values were calculated by two-tailed Student *t*-test. n.s. = non-significant.

Fig. 2). We then focused our analysis on the subset of miRNAs that are misregulated in *alg-1(gk214)* mutants (Fig. 2b). In *dpf-3(xe68);alg-1(gk214)* animals, we observed that 55 out of those 75 miRNAs (73.3%) fall within the two-fold threshold and thus also had similar steady-state to WT and *dpf-3(xe68)* animals. This suggests that the suppression of defective miRNA-pathway-related phenotypes of *dpf-3(xe68);alg-1(gk214)* animals also extrapolates to the miRNA molecular level.

Interestingly, some let-7 miRNA family members were found to be downregulated in *alg-1(gk214)* compared to WT, while they were all normally expressed in the double mutant according to our small RNA sequencing data (Fig. 2b). We measured their abundance using RT-qPCR and confirmed that *dpf-3(xe68);alg-1(gk214)* young adults have similar let-7 family miRNA levels to WT animals, contrasting the reduced miRNA levels of *alg-1(gk214)* animals (Fig. 2c). Then, we verified whether *dpf-3(xe68);alg-1(gk214)* animals could achieve proper target silencing. RT-qPCR data of known let-7 targets (DAF-12 and HBL-1 mRNAs)[41–43] show that *dpf-3(xe68);alg-1(gk214)* young adults have expression levels of those targets similar to WT animals, in opposition to *alg-1(gk214)* derepressed target levels (Fig. 2d). This suggests that the restored level of let-7 miRNA family members re-establishes normal miRNA target repression in *dpf-3(xe68);alg-1(gk214)* animals. Altogether, these results indicate that the rescue of *alg-1(gk214)*-related phenotypes is due to a restoration of proper miRNA-mediated gene silencing caused by the loss of *dpf-3*.

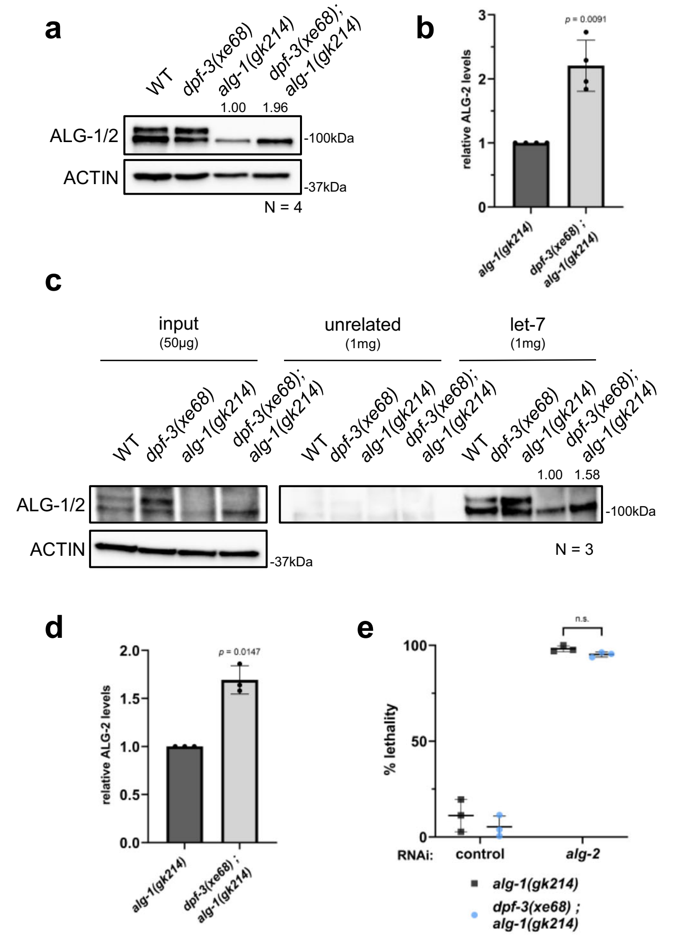

Fig. 3 | ALG-2 compensates for the loss of ALG-1 in *dpf-3(xe68);alg-1(gk214)* animals. a Representative western blot of ALG-1/2 protein expression in WT, *dpf-3(xe68), alg-1(gk214)* and *dpf-3(xe68);alg-1(gk214)* worms. ACTIN acts as a loading control. The numbers on top of the *alg-1(gk214)* and *dpf-3(xe68);alg-1(gk214)* bands represent ALG-2 protein signal intensity relative to *alg-1(gk214)* when normalized on the ACTIN band. *N* = 4. **b** Quantification of the signal intensity of the ALG-2 western blot band across four biological replicates, comparing *alg-1(gk214)* condition to *dpf-3(xe68);alg-1(gk214)* condition. Data are presented as mean values of four biological replicates (black dots) ± SD. *P*-value was calculated by two-tailed one sample Student *t*-test. **c** let-7 miRISC purification was performed and followed by western blot analysis to measure ALG-1/2 protein association to let-7. The western blot shown is a representative replicate. Input and purifications are separated as they received different exposure time, but were still ran on the same gel. The numbers on top of the *alg-1(gk214)* and *alg-1(gk214); dpf-3(xe68)* bands in the let-7 section represent ALG-2 protein signal intensity relative to *alg-1(gk214). N* = 3. **d** Quantification of the signal intensity of the ALG-2 western blot band of the let-7 miRISC purifications across three biological replicates, comparing *alg-1(gk214)* condition to *dpf-3(xe68);alg-1(gk214)* condition. Data is presented as mean value of three biological replicates (black dots) ± SD. *P*-value was calculated by two-tailed one sample Student *t*-test. **e** *alg-2* RNAi was performed on *alg-1(gk214)* and *alg-1(gk214); dpf-3(xe68)* L4 animals (5–10 animals per condition per replicate) and the percentage of lethality in the progeny was measured (approx. 100 progeny per condition per replicate). Data are presented as mean values ± SD of three biological replicate. Each dot represents an independent experiment. *P*-value was calculated by two-way ANOVA. n.s. = non-significant.

Depleting DPF-3 increases ALG-2 functional miRISC

As ALG-2 constitutes the other main miRNA-specific Argonaute, we next asked if the loss of *dpf-3* could influence its function. We first explored the effect of *dpf-3* loss on ALG-2 protein level. Although the loss of *dpf-3* alone does not appear to affect ALG-2, we detected a significant increase in its level in the *dpf-3(xe68);alg-1(gk214)* double mutant animals (Fig. 3a, b) when compared to *alg-1(gk214)* animals baseline level. Next, we examined if the noted ALG-2 accumulation leads to more miRISC formation. To test this, we purified let-7 miRISC using a biotinylated complementary let-7 oligonucleotide and monitored ALG-2 by western blot[44]. We observed an increase in ALG-2 association to let-7 in *dpf-3(xe68);alg-1(gk214)* animals compared to *alg-1(gk214)* (Fig. 3c, d), suggesting that ALG-2 miRISC is formed more readily and is more likely able to repress its let-7 miRNA targets in the absence of *dpf-3* in *alg-1* loss-of-function animals. To determine if this effect is specific to let-7 miRISC or broader, we purified miR-77 miRISC, another miRNA which also has its level re-established by the loss of *dpf-3* in *alg-1(gk214)* animals (Fig. 2b). As for let-7, we also observed an increase in miR-77 association to ALG-2 in *dpf-3(xe68);alg-1(gk214)* animals compared to *alg-1(gk214)* alone (Supplementary Fig. 3a, b), confirming that the increase of active ALG-2 miRISC is broader than a single miRNA family. Overall, those results indicate that knockout of *dpf-3* allows ALG-2 to compensate for the lack of its paralog ALG-1 in the miRNA pathway by increasing its expression and association with miRNAs to produce functional miRISC.

To next verify that ALG-2 is essential for the rescue, and not another Argonaute that could assume a non-canonical function under these specific conditions, we performed ALG-2 RNAi on *dpf-3(xe68);alg-1(gk214)* worms and scored lethality. We observed that the loss of both miRNA-specific Argonautes remained lethal (Fig. 3e), confirming that ALG-2 is essential to suppress the loss of ALG-1 in the absence of DPF-3. Additionally, we investigated if *dpf-3* and *alg-2* genetically interact together by crossing a strain carrying the *alg-2(ok304)* loss-of-function allele with our *dpf-3(xe68)* strain and verified for genetic synergy. We assessed both the alae gap and bursting through the vulva phenotypes and could not see any synergistic effect for those (Supplementary Fig. 4a, b). We also performed miRNA sequencing and did not observe any differences in miRNA expression when comparing *dpf-3(xe68);alg-2(ok304)* animals to single mutants (Supplementary Fig. 4c). This emphasizes that the modulatory effect of DPF-3 in the miRNA pathway is only unveiled in absence of ALG-1.

The DPF-3 dipeptidase activity appears not to be contributing to ALG-2 modulation

As ALG-2 is essential for the suppression of *alg*-1-related miRNA defects in *dpf-3* loss-of-function animals, we next tackled the question of how DPF-3 could regulate ALG-2. DPF-3 being a dipeptidyl peptidase, we verified if it could cleave an ALG-2 N-terminal dipeptide to regulate its function. ALG-2 amino acids sequence possesses two different isoforms with two distinct N-termini resulting from the alternative splicing of a 5′ exon of ALG-2 mRNA. The more expressed shorter isoform notably possesses a proline at the second position from the N-terminus, making this isoform a likely candidate for DPF-3 processing. The longer isoform also contains a proline but at the third position, making this isoform a less likely substrate for DPF-3 processing.

We first used a proteomic approach called Terminal Amine Isotopic Labelling of Substrates (TAILS) combined with liquid chromatography and tandem mass spectrometry (LC/MS-MS)[45,46] to verify if we could detect a cleavage (or a lack of it) in WT and *dpf-3(xe68)*. This method has been applied for protein N-terminal characterization and quantification by filtering out tryptic peptides to enrich both the natural and neo-N-termini of proteins produced from proteolysis[47]. We used this method with total extracts of WT and *dpf-3(xe68)* worms and searched for peptides of ALG-2 (Supplementary Fig. 5a). We could confirm the enrichment worked as we detected a high number of peptides specific to the samples treated with the TAILS polymer compared to the preTAILS control samples (Supplementary Fig. 5b). Unfortunately, we could not find any ALG-2 peptides enriched by TAILS, but we did identify a potential natural substrate of DPF-3 in CCT-4 where the cleavage after the proline at the third position from the N-terminus is 88-fold enriched in WT conditions compared to *dpf-*

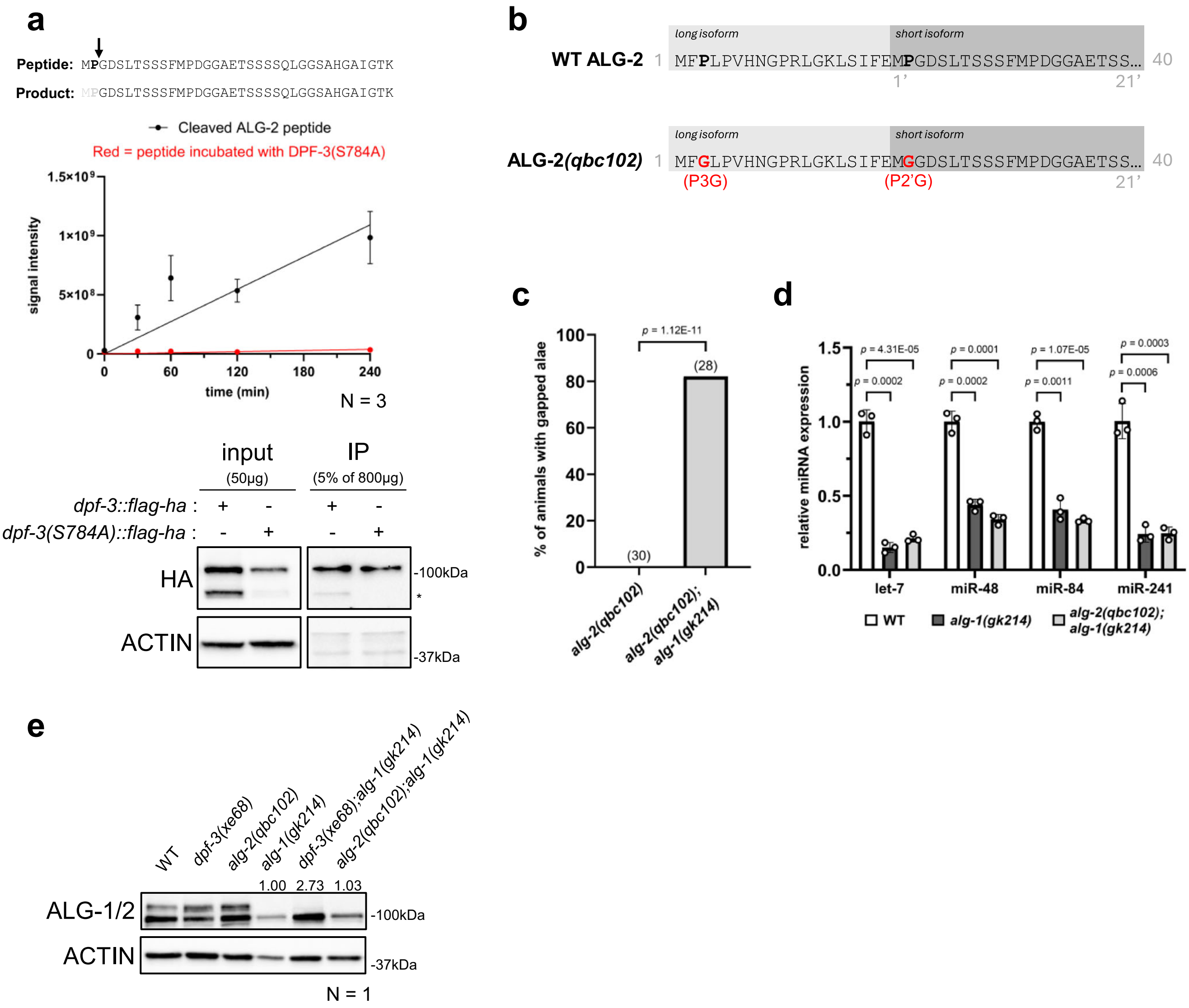

Fig. 4 | DPF-3 dipeptidase activity is not contributing to ALG-2 modulation. **a** Linear regression of the measured signal intensity of the synthetic ALG-2 N-terminal peptide over time after processing by LC-MS/MS. The detected peptide sequences are listed on top of the graph with the black arrow pointing at the cleavage site. The signal intensity was normalized with a CytC peptide. The red line shows signal intensity of cleaved peptide when incubated with catalytic dead DPF-3. Data are presented as mean values of signal intensity for each time point ± SD. The western blot analysis depicts a representative purification of either wild-type or catalytic dead DPF-3 for incubation with ALG-2 peptide. *N* = 3. **b** Schematic of ALG-2 N-terminal protein sequence and the result of the proline mutations inserted by CRISPR-Cas9. **c** Percentage of proline mutant animals displaying gaps in their alae structure at 20 °C. The numbers on top of the bars in the graph represent the number of animals scored for each genotype. *P*-value was calculated by two-sided Fisher’s exact test. **d** RT-qPCR was performed on total RNA extracts of WT, *alg-1(gk214)* and *alg-2(qbc102);alg-1(gk214)* worms to measure the relative expression of the let-7 miRNA family members. Data are presented as mean values of 3 biological replicates (white dots) ± SD. MiRNA levels were normalized using sn2841. *P*-values were calculated by two-tailed Student *t*-test. n.s. = non-significant. **e** Western blot of ALG-1/2 protein expression in WT, *dpf-3(xe68), alg-2(qbc102), alg-1(gk214), dpf-3(xe68);alg-1(gk214)* and *alg-2(qbc102);alg-1(gk214)* animals. ACTIN acts as a loading control. The numbers on top of the *alg-1(gk214), alg-1(gk214); dpf-3(xe68)* and *alg-2(qbc102);alg-1(gk214)* bands represent ALG-2 protein signal intensity relative to *alg-1(gk214)* when normalized on the ACTIN band.

3(xe68) (Supplementary Fig. 5c). This suggests that validating the N-terminal sequence of ALG-2 using proteomics will be challenging.

Therefore, we used an in vitro setting to verify if DPF-3 can in fact cleave an ALG-2 N-terminal peptide. We conducted an in vitro cleavage assay using a synthetic peptide representing the N-terminus of ALG-2’s short isoform incubated with affinity purified WT or catalytic dead DPF-3 protein (DPF-3(S784A))[34]. We then measured the accumulation of the product peptide, which should be missing its first two amino acids, using liquid chromatography followed by tandem mass spectrometry (LC-MS/MS). The in vitro assay showed that the ALG-2 N-terminus is actively being cleaved by DPF-3 as we could detect an increase in cleaved peptide over time when incubated with wild-type DPF-3, and not with DPF-3(S784A) (Fig. 4a). We also performed a control assay with a peptide in which the proline at the second position was substituted with glycine, making it resistant to cleavage[34]. We could not detect cleavage with this amino acid substitution (Supplementary Fig. 6a), indicating that DPF-3 needs a second position proline to produce cleaved ALG-2 peptide. This result shows that ALG-2 is a DPF-3 substrate for dipeptide cleavage in vitro.

We then moved to an in vivo setting to verify if the lack of ALG-2 N-terminal dipeptide cleavage is the mechanism implicated in the rescue of miRNA defects seen in *dpf-3(xe68);alg-1(gk214)* animals. We first tested if the DPF-3 catalytic mutant phenocopies the loss of DPF-3 in animals missing ALG-1. When crossed into the *alg-1* loss-of-function

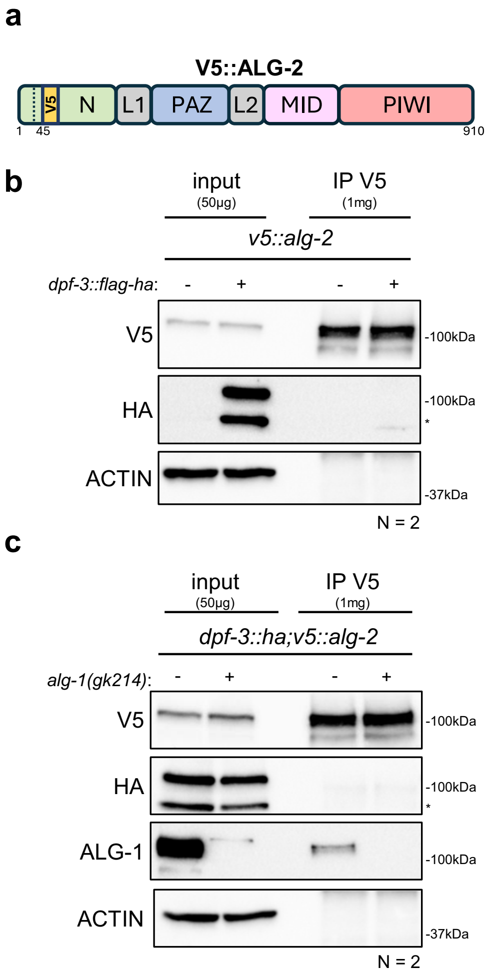

Fig. 5 | DPF-3 does not co-immunoprecipitate with ALG-2. a Schematic of endogenously V5 tagged ALG-2 protein by CRISPR-Cas9. The V5 tag is represented in yellow. Amino acids position are displayed at the bottom. **b** Representative western blot of V5::ALG-2 immunoprecipitation in *v5::alg-2* (- lanes) or *dpf-3::flag-ha;v5::alg-2* (+ lanes) background. The asterisk highlights a DPF-3 isoform of lower molecular weight than expected. ACTIN acts as a loading control. *N* = 2. **c** Representative western blot of V5::ALG-2 immunoprecipitation in *dpf-3::flag-ha;v5::alg-2* (- lanes) or *dpf-3::flag-ha;v5::alg-2;alg-1(gk214)* (+ lanes) background. The asterisk highlights a DPF-3 isoform of lower molecular weight than expected. ACTIN acts as a loading control. *N* = 2.

background, the catalytic mutant failed to rescue the miRNA pathway at all levels: alae formation (Supplementary Fig. 6b), *let-7* miRNA family level (Supplementary Fig. 6c) and ALG-2 protein level (Supplementary Fig. 6d). To get further insights, we endogenously mutated both ALG-2 isoforms' N-terminal prolines to glycine using the CRISPR-Cas9 methodology, thereby making ALG-2 resistant to potential cleavage as seen in our in vitro assay (Fig. 4b). We crossed this newly generated allele into *alg-1(gk214)* background and tested if the mutation of both prolines was enough to rescue the phenotypes. We observed that this proline mutant strain did not phenocopy the rescue of *alg-1(gk214)* alae gaps, let-7 miRNA family levels, and ALG-2 protein abundance that arises from the complete loss of *dpf-3* (Fig. 4c–e). However, it is worth mentioning that mutating both N-terminal prolines appears to affect ALG-2's functionality, as animals with this *alg-2* allele in *alg-1(gk214)* background show a very high proportion of gapped alae (Fig. 4c). This could limit our ability to detect phenotype suppression even in the occurrence of a dipeptide retainment. Altogether, these results show that while DPF-3 can cleave a N-terminal dipeptide of ALG-2 in vitro, we found no evidence of cleavage in vivo, using both genetic and proteomic approaches, suggesting that DPF-3 regulates the microRNA pathway independently of ALG-2 N-terminus processing.

DPF-3 does not stably bind to ALG-2

We next aimed to understand how DPF-3 acts on ALG-2 to allow phenotypical and molecular rescues to occur independently of DPF-3's catalytic activity. Recent studies demonstrated that dipeptidyl peptidases could sequester their substrate simply by interaction and without catalytic activity[48,49]. Therefore, we first asked if DPF-3 can physically interact with ALG-2 as seen with ALG-1 (Fig. 1a). Since we are not able to get an ALG-2-specific antibody due to its high similarity with ALG-1, we endogenously tagged *alg-2* using CRISPR-Cas9 methodology. This proved to be challenging as we could not insert a tag at the very N-terminus of ALG-2 as commonly done for Argonaute proteins because dipeptidyl peptidases mainly act on this part of their substrates[31,32,33]. Moreover, since we are working in an *alg-1* loss-of-function background, we needed to create a functional tagged ALG-2 protein to avoid lethality. Thus, we used AlphaFold's[50] ALG-2 structure prediction and identified a suitable region further into the N domain for tagging ALG-2 with a V5 tag (Fig. 5a). Our strategy has been fruitful as we isolated *alg-1(gk214)* animals expressing V5::ALG-2, confirming that endogenously tagged V5::ALG-2 is functional. The immunoprecipitation experiments we performed show that DPF-3 does not co-immunoprecipitate with ALG-2 (Fig. 5b). Since DPF-3's effect on the miRNA pathway is most noticeable in an *alg-1* loss-of-function background, we also performed immunoprecipitations with samples of animals lacking *alg-1* to verify if DPF-3 would start to interact with ALG-2 in this condition. We still could not detect any co-immunoprecipitation between them even in *alg-1(gk214)* background (Fig. 5c). We additionally did the reverse experiment where we instead immunoprecipitated DPF-3 and verified for ALG-2 enrichment, but the result remained the same (Supplementary Fig. 7a). To further confirm, we carried out ALG-2 immunoprecipitation treated with either RNase inhibitors or RNase and performed mass spectrometry on the samples. Both conditions also reveal that DPF-3 does not co-immunoprecipitate with ALG-2 (Supplementary Fig. 7b, c). Finally, we also performed a V5::ALG-2 immunoprecipitation to verify if the catalytic mutant of DPF-3 would now quench ALG-2, but we still could not detect any co-immunoprecipitation between the two proteins (Supplementary Fig. 7d). Those results demonstrate that DPF-3 does not appear to bind stably to ALG-2 and impair its ability to perform its function. As such, this also indicates that while DPF-3 can play a role in multiple small RNAs pathway[34], it is not a general binding partner of miRNA-specific Argonautes and instead favors interaction with ALG-1 under normal conditions (as seen in Fig. 1a).

Absence of DPF-3 in *alg-1(gk214)* background leads to an increase in ALG-2 mRNA

As we detected a significant increase in ALG-2 protein level in the absence of both DPF-3 and ALG-1 and considering that this does not appear to be caused by a stabilization of the protein lacking an N-terminus dipeptide cleavage, we next investigated if the loss of DPF-3 could influence the production of ALG-2 mRNA. We first performed RT-qPCR using primers in exon junctions of the ALG-2 mRNA to check for the level of mature mRNA. The result showed that *dpf-3(xe68);alg-1(gk214)* double mutant animals have an increase of more than 1.5-fold in mature ALG-2 mRNA relative to WT animals, while *dpf-3(xe68)* and *alg-1(gk214)* worms have no significant difference (Fig. 6a). We speculated that the increase in ALG-2 mRNA could be an indirect effect of the decreased endogenous siRNAs activity in *dpf-3* mutants described by Gudipati et al., where loss of *dpf-3* mainly reduces WAGO-3 stability and causes defective siRNA sorting[34]. It is possible that 22G-RNAs normally target ALG-2 mRNA to regulate its expression and that removing *wago-3* (mimicking the effect of *dpf-3* mutation) from the

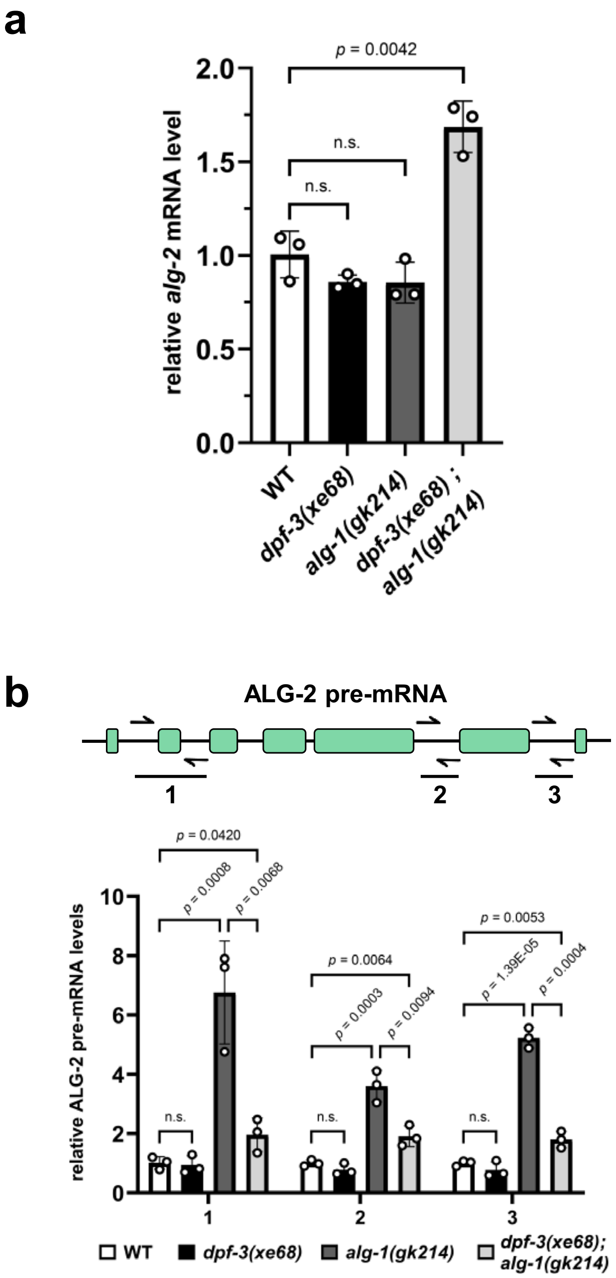

Fig. 6 | Absence of DPF-3 in *alg-1* loss-of-function animals increases ALG-2 mRNA abundance. a RT-qPCR performed on total RNA extracts of WT, *dpf-3(xe68)*, *alg-1(gk214)* and *dpf-3(xe68);alg-1(gk214)* animals to measure mature ALG-2 mRNA using primers in exon-exon junctions. Data are presented as mean values of 3 biological replicates (white dots) ± SD. ALG-2 mRNA levels were normalized using *tba-1*. *P*-values were calculated by two-tailed Student *t*-test. n.s. = non-significant. **b** Top: schematic of ALG-2 unspliced mRNA where half-arrows represent roughly the position and orientation of the primers used for qPCR. Bottom: RT-qPCR performed on total RNA extracts of WT, *dpf-3(xe68)*, *alg-1(gk214)* and *dpf-3(xe68);alg-1(gk214)* animals to measure ALG-2 precursor mRNA using primers in intronic regions. Data are presented as mean values of 3 biological replicates (white dots) ± SD. ALG-2 pre-mRNA levels were normalized using *tba-1*. *P*-values were calculated by two-tailed Student *t*-test. n.s. = non-significant.

genetic background in combination with *alg-1(gk214)* mutation could replicate the suppression through increased ALG-2 abundance. Hence, we crossed animals carrying the *wago-3(tm1120)* loss-of-function allele with *alg-1(gk214)* animals to generate a double mutant strain and verified if this was sufficient for defective miRNA pathway-related phenotypes rescue. *Wago-3(tm1120);alg-1(gk214)* worms did not display an increase in general fitness and showed a bursting rate just under 20% when maintained at the restrictive temperature (Supplementary Fig. 8), akin to what is observed in *alg-1(gk214)* animals (Fig. 1d). We conclude that a change in the functionality of the *C. elegans*-specific WAGOs siRNA pathway caused by the *dpf-3* mutation is likely not the reason for the observed increase of ALG-2 mRNA level in *dpf-3(xe68);alg-1(gk214)* animals.

We next asked if the loss of *dpf-3* could affect the abundance of the ALG-2 precursor mRNA by affecting its transcription and/or splicing using RT-qPCR. While *dpf-3(xe68)* did not affect the pre-mRNA level, *dpf-3(xe68);alg-1(gk214)* animals showed a consistent increase of about 2-fold compared to WT worms (Fig. 6b). *Alg-1(gk214)* animals also displayed a greatly variable increase in ALG-2 pre-mRNA levels but, contrary to double mutant animals, this did not lead to increased mature mRNA levels (Fig. 6a, b). Additionally, we tested if this effect is specific to ALG-2 by monitoring stable and commonly used reference genes, *pmp-3* and *cdc-42*[51]. While *alg-1(gk214)* worms also displayed a significant increase in PMP-3 pre-mRNA, double mutant animals remained at WT levels (Supplementary Fig. 9a). We observed a slight increase in mature PMP-3 mRNA in *dpf-3(xe68);alg-1(gk214)* worms (Supplementary Fig. 9b), but far from the increase we observed in the case of ALG-2 mRNA. Similarly, *alg-1(gk214)* animals had an increase in CDC-42 pre-mRNA but not double mutants (Supplementary Fig. 7c). However, for CDC-42 specifically, *alg-1(gk214)* worms had a significant increase in mature mRNA and *dpf-3(xe68);alg-1(gk214)* had only a slight increase (Supplementary Fig. 9d). This suggests that, for some genes, the removal of *alg-1* alone is sufficient to increase mature mRNA expression, but for other genes such as *alg-2*, *dpf-3* must also be absent. Altogether, these results show that *dpf-3* knockout in *alg-1(gk214)* background increases in the animal's ability to produce mature ALG-2 mRNA.

Discussion

As miRNA-specific Argonaute proteins constitute the main components of a key regulatory pathway for many essential biological processes, they must be tightly regulated for the organisms to develop normally and maintain homeostasis. Our results uncovered a new interactor and regulator of the miRISC in *C. elegans*, namely the dipeptidyl peptidase DPF-3. We demonstrated with our genetic and molecular data that a loss of function of *dpf-3* removes an inhibition of *alg-2* that enables this Argonaute protein to better compensate for a loss of function of its paralog *alg-1*. Mechanistically, several pieces of data presented here indicate that the dipeptidyl peptidase activity of DPF-3 does not contribute to regulate *alg-2*. First, even though DPF-3 can cleave a N-terminal ALG-2 dipeptide in vitro, we could not validate that this processing happens in vivo or detect a stable interaction between ALG-2 and DPF-3, in contrast to what was observed for WAGO-1 and WAGO-3[34]. Second, animals expressing either an ALG-2 prolines variant or a DPF-3 catalytic mutant failed to rescue *alg-1*-loss-of-function-related defects at the phenotypical and molecular level. Altogether, this suggests that N-terminal processing of ALG-2 is not the mechanism used by DPF-3 to regulate ALG-2. The reason why ALG-2's N-terminus might not be available for DPF-3 cleavage in vivo could be related to the tendency of AGOs' N-terminal region to be unstructured and to fold over other domains as observed in humans[27]. Furthermore, the N domain is highly variable in composition among AGOs and this allows unique interactions with specific proteins as seen for AGO1 in plants[52,53] and for ALG-1 in worms[54,55]. This could explain why DPF-3 holds an exclusive stable interaction with ALG-1 and not ALG-2. Taken together, those properties could make the N-terminus of ALG-2 not available for processing depending on the context. This highlights some limitations of our study, as all our data focused on visible phenotypes that occurred at a specific developmental stage (i.e. larvae to young adult transition) and was generated using total extracts. This

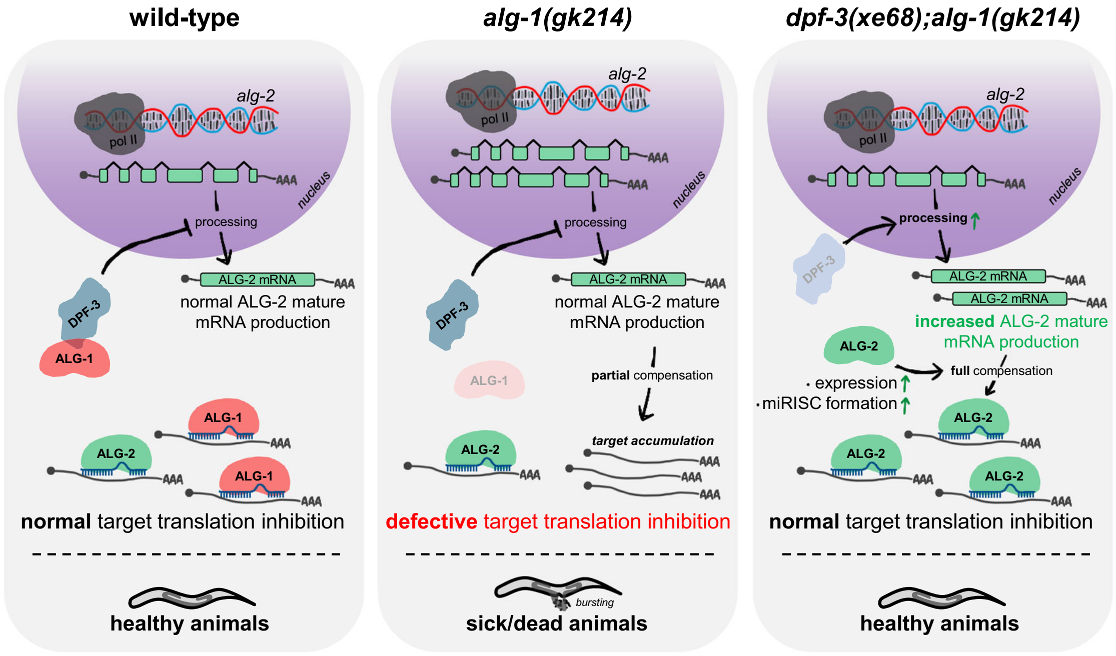

Fig. 7 | Model of DPF-3's regulation on the interplay between miRNA-specific Argonautes. In wild-type genetic background, DPF-3 favors interaction with ALG-1 and maintains a normal transcription/splicing rate of ALG-2 mRNA. This allows ALG-1 to assume the bulk of the miRNA gene regulatory function, achieving normal target translational inhibition and keeping the animals healthy. In *alg-1(gk214)* genetic background, ALG-2 pre-mRNA starts to accumulate but DPF-3 limits its processing, which impedes it to compensate for the absence of ALG-1, leading to target mRNAs misregulation and appearance of deleterious phenotypes. In *dpf-3(xe68);alg-1(gk214)* conditions, DPF-3's negative regulation of ALG-2 mRNA processing is relieved and allows it to compensate for the lack of ALG-1 by increased protein abundance and increased active miRISC formation. ALG-2 can now maintain proper target translational inhibition and keep the animals healthy again.

possibly hindered our ability to detect instances where ALG-2 regulation by the dipeptidase activity of DPF-3 could be tissue and/or stage-specific, where it acts on ALG-2's N-terminus only in specific cells at a certain time point. This would make it hard to detect using our methods. Regardless, our data instead suggest a role that is independent of DPF-3's catalytic capabilities for the regulation of ALG-2, such as control of the maturation of ALG-2 mRNA following its increase in transcription in *alg-1* loss-of-function background.

The dynamic between paralogs of miRNA-specific Argonautes during development in both *C. elegans* and mammals has been an interesting subject for several years. An early study conducted in mouse embryonic stem cells demonstrated that re-introducing any of the four miRNA-specific AGO in AGO1-4 knockout cells is sufficient to rescue apoptosis, pointing out that all mammalian AGOs contribute to miRNA function, but that they also have largely overlapping functions in this pathway[56]. On *C. elegans*' side, previous studies have reported that ALG-1 is the major contributor to the miRNA pathway as only *alg-1* loss-of-function mutant animals display developmental defects[19]. These observations indicate that miRNA-specific Argonautes can compensate for one another, although in *C. elegans* ALG-2 can only perform it to a lesser extent. Since ALG-1 and ALG-2 own a similar expression pattern[16,17] and bind a high proportion of the same miRNAs[20,57], ALG-2 appears to possess the required flexibility to compensate for the lack of its paralog. So why is ALG-2 unable to do it? We propose a model where DPF-3 can be an important factor in the regulation of the interplay between ALG-1 and ALG-2, mainly when it would be necessary for ALG-2 to assume the bulk of the miRNA function in the absence of ALG-1 (Fig. 7). We postulate that DPF-3 contributes to miRNA-mediated gene regulation in one main aspect: control of ALG-2 mRNA production. In WT animals, DPF-3 interacts with ALG-1 and exerts its yet unknown regulatory functions on this Argonaute protein. Additional experiments using other mild *alg-1* alleles (such as recently found antimorphic alleles[58]) will be necessary to define precisely how DPF-3 affects ALG-1 in the absence of ALG-2. Our data also demonstrate that DPF-3 limits ALG-2 contribution to the miRNA pathway not through dipeptidase activity nor interaction but by affecting the processing of its mRNA. In *alg-1(gk214)* background, the physical interaction of DPF-3 with ALG-1 is relieved and animals start to accumulate ALG-2 pre-mRNA through altered transcriptional gene silencing mechanisms. The presence of DPF-3 hinders the production of mature mRNA, possibly through negative regulation of an unknown protein such as a transcription or splicing factor. Due to these actions of DPF-3, ALG-2 is unable to fully compensate for the absence of ALG-1, leading to miRNA targets accumulation and poor animal fitness. In absence of *dpf-3*, both ALG-2 mature mRNA and protein levels are increased, leading to abundant active miRISC that can fully compensate for the miRNA function.

The *alg-1(gk214)* allele used throughout this study is a standard, well-established loss-of-function allele for assessing *alg-1* function in the miRNA pathway[16,20,59]. As there are other *alg-1* loss-of-function alleles with well-defined phenotypes, such as *alg-1(tm492)*[58], we tested whether the loss of *dpf-3* could also suppress miRNA-related defects of this other loss-of-function allele. In this case, *dpf-3(xe68)* did not suppress the phenotype (Supplementary Fig. 10a), suggesting that the suppressive properties of *dpf-3* loss-of-function may be allele-specific. We hypothesize that this could result from the different putative peptides produced by each allele, where *alg-1(gk214)* causes a frameshift and an early stop codon in the N domain, while *alg-1(tm492)* involves a large deletion further down the gene that could generate a truncated ALG-1 peptide with a mostly intact N domain (Supplementary Fig. 10b). As previously stated, the N-terminal domain of Argonautes serves as an important regulatory hub. Thus, it is possible that the putative peptide of *alg-1(tm492)* retains interaction with regulators, unlike *alg-1(gk214)*, which might explain the different outcomes of genetic interaction seen with *dpf-3*. This represents a limitation of our study, as further experiments with other putative *alg-1* loss-of-function alleles will be needed to directly test this hypothesis.

A surprising result brought by our study is the increase in precursor mRNAs (pre-mRNAs) that appears to happen broadly in *alg-1(gk214)* animals (Fig. 6b and Supplementary Fig. 9a, c). This suggests that the loss of function of *alg-1* can alter broad transcriptional gene silencing mechanisms that are in place. However, it seems that this mutation is not enough to cause an increase in end product in most cases, as only *cdc-42* had an increase in mature mRNA in *alg-1(gk214)* background by itself. Interestingly, loss of *dpf-3* apparently helps animals to process the large increase of pre-mRNAs seen in *alg-1(gk214)* into mature mRNAs, albeit only slightly for PMP-3 and CDC-42. This could be a result of a negative regulation of transcription and/or RNA processing factors by DPF-3 that is removed with *dpf-3* null. In fact, this kind of mechanism is not unknown to dipeptidyl peptidases function: absence of DPP9 (ortholog of DPF-3) leads to stabilization of the epithelial-to-mesenchymal transcription factor ZEB1, and, in this case, this participates in increased tumorigenesis and metastasis in breast cancer[60]. Thereby, it is possible that loss of *dpf-3* in *alg-1* loss-of-function background relieves negative regulation of ALG-2 mRNA processing, which in turn could help produce more protein to achieve *alg-1*-related phenotypes suppression.

In summary, this study uncovers DPF-3 as a regulator of the miRNA Argonautes. Lifting the negative regulation of DPF-3 on ALG-2 in animals that struggle to achieve proper miRNA gene regulatory function, such as *alg-1* loss-of-function animals, is very beneficial for animal fitness. This demonstrates that DPF-3 participates in gatekeeping the compensation of miRNA-specific Argonaute ALG-2 when ALG-1 cannot perform its duty. Further studies will be necessary to fully comprehend how DPF-3 can regulate the proper functioning of the miRNA pathway in *C. elegans*, and it would warrant investigation of whether this conserved dipeptidyl peptidase can control miRNA-specific Argonautes in mammals.

Methods

C. elegans strains

C. elegans strains were cultured under standard conditions[61]. Strains were maintained at 15 °C on Nematode Growth Media (NGM) plates and fed *E. coli* strain OP50. Worms used for experiments were switched at 25 °C unless stated otherwise. All strains used for this project are listed in Supplementary Data 1.

Preparation of protein extracts

For ALG-1/ALG-2 MS. Synchronized L1 worms were plated onto 2% NGM plates containing NA22 bacteria as a food source and collected at the specified developmental stages. The worms were washed three times with M9 buffer and transferred to 2 mL tubes) containing Zirconia/Silica beads (Biospec) in lysis buffer (50 mM Tris-HCl, pH 7.5, 150 mM NaCl, 1% Triton X-100, 1 mM EDTA). The buffer was supplemented with 1 mM PMSF and one tablet of cOmplete Protease Inhibitor (Roche) per 50 mL. Worm lysis was performed using an MP Biomedicals Fast Prep-24 5 G bead beater for 16 cycles at 8 m/sec. The lysate was then centrifuged at 16,100 g for 10 min at 4 °C. The supernatant was collected into a fresh tube, and protein concentration was determined using the standard Bradford assay. **For pulldowns and V5 IPs**: Extracts were prepared from ~100,000 synchronized young adult animals. Worms were washed and resuspended in lysis buffer (100 mM Potassium Acetate, 30 mM Hepes-Potassium Hydroxide pH 7.4, 2 mM Magnesium Acetate, 1 mM DTT, 0.5% triton, 2% RNase inhibitors and protease inhibitors) before being extracted with a Bullet Blender Storm24 (NextAdvance) for 5 min at maximum intensity. The extracts were centrifugated at 13,000 x *g* for 15 min at 4 °C and the clarified supernatants were collected. Protein concentration was quantified using standard Bradford protocol. **For ALG-1/2 western blots**: 50 worms for each genotype were single-picked and boiled at 99 °C for 10 min in lysis buffer supplied with SDS loading buffer (10 mM Tris-HCl [pH 6.8], 2% [w/v] SDS, 100 mM DTT and 10% [v/v] glycerol). The extracts were then directly loaded onto a polyacrylamide gel for electrophoresis.

Protein immunoprecipitation

Proteins of interest were immunoprecipitated using either Anti-FLAG M2 Magnetic Beads (Sigma-Aldrich) or Dynabeads protein G (Invitrogen) coupled with anti-V5 tag antibody (Abcam ab27671). 2 mg of protein extract of the specified worm genotypes was incubated for 2 h at 4 °C with 20 μL of previously thrice washed beads with TBS (50 mM Tris-HCl, 150 mM NaCl) in a total volume of 500 μL. Bound beads were then washed three more times using lysis buffer and finally resuspended in 4X SDS loading buffer for western blot analysis.

Mass spectrometry to characterize ALG-1 and ALG-2 complex

Upon IP as described above, 5.0 μl of digestion buffer (3 M GuaHCl (Guanidine Hydrochloride), 20 mM EPPS (4-(2-Hydroxyethyl)-1-piperazinepropanesulfonic acid) pH 8.5, 10 mM CAA (2-Chloroacetamide), 5 mM TCEP (Tris(2-carboxyethyl)phosphine hydrochloride)) and 1.0 μl of Lys-C (0.2 μg/μl in 50 mM Hepes, pH 8.5) was added to the beads for incubation at 21 °C for 2–4 h while shaking. Subsequently, 17.0 μl of 50 mM HEPES, pH 8.5 and 1.0 μl of 0.2 μg/μl trypsin were added and incubation continued at 37 °C overnight. In the morning, another 1.0 μl of trypsin was added and incubation continued for 4 more hours. Generated peptides were analyzed by LC-MS on an LTQ Orbitrap Fusion (Thermo Fisher Scientific) with Easy-nLC and 75μm × 2 cm PepMap Trap (213769) and 50μm × 15 cm ES901 C18 (215081) columns. The following gradient was used: 0–3 min 2–6% B in A, 3–43 min 6–22%, 43–52 min 22–28%, 52–60 min 28-36%, 60–61 min 36–80%, 61–75 min 80%. A: 0.1%FA in H_2O; B: 0.1%FA in MeCN. Mascot was used to search the CAEEL subset of the UniProt. A threshold value (FDR) of 0.05 and S0 (curve bend) of 2.0 were used. Results were exported from Perseus and visualized using statistical computing language R. For each pairwise group comparison, log-2-transformed feature quantification values for all features to be tested for differential expression were passed to function lmFit() from R/Bioconductor package limma, yielding a model that benefits from limma-based information sharing between features. Models were then interrogated by passing appropriate contrasts to limma::contrasts.fit(), summary statistics therefrom were moderated using limma::eBayes(), and the results of the differential expression tests for all features were compiled with limma::topTable(..., number = Inf).

Imaging and microscopy

DIC images of alae and GFP fluorescence of seam cells were taken with a Zeiss AxioCam HRm digital camera mounted on a Zeiss Axio Imager M1 microscope. Images of *scmp::gfp* animals were fused together in a panorama using the ZEN software. Images were taken using the same settings and exposure time for each animal (80 ms exposure for DIC channel and 125 ms exposure for GFP channel). GFP pixel intensity was optimized for better viewing using the ZEN software.

Seam cells numbering

L1 worms of the specified genotypes were placed on NGM plates at 25 °C and grown until the gravid adult stage. Worms were then placed and drugged using 1 mM levamisol on a 2% [w/v] agarose pad thinned on a standard microscopy slide. Number of seam cells was counted using the GFP channel of a Zeiss Axio Imager M1 microscope.

Alae phenotype scoring

L1 worms of the specified genotypes were placed on NGM plates at 20 °C and grown until the young adult stage. Worms were then placed and drugged using 1 mM levamisol on a 2% [w/v] agarose pad thinned on a standard microscopy slide. Alae integrity was verified with DIC microscopy.

Bursting phenotype scoring

Adult worms of the specified genotypes were placed on NGM plates at 25 °C for 24 h before being removed. The bursting phenotype of the progeny was scored 72 h later.

RNA extraction

RNA was extracted by classical Trizol/Chloroform method from young adult worm populations in triplicate for each different genetic background assessed. Briefly, the worms were collected in M9 saline solution, and 4 volumes of TRI reagent (Sigma-Aldrich) was added. The samples were then vortexed for 30 s, flash frozen with liquid nitrogen and thawed at 37 °C four times successively. Another 2 volumes of TRI reagent were then added before vortexing for another 30 s. A quarter of total volume of chloroform was then added to the samples and was thoroughly mixed before centrifugation at 15,000 × *g* for 15 min at 4 °C. The aqueous phase was collected and precipitated overnight at −20 °C with 2 volumes of 95% ethanol. After precipitation, the samples were centrifugated at 17,000 × *g* for 15 min at 4 °C and the pellet was washed once with 75% ethanol. The pellet was dried under a chemical hood for 10 min and was finally resuspended in RNase-free H_2O.

Quantitative reverse-transcription PCR (RT-qPCR)

The RNA was reverse transcribed with Multiscribe reverse transcriptase (Thermo Fisher Scientific). TaqMan probes specific for the assessed miRNAs were used for the measurement of miRNA levels, and SYBR green master mix (Biorad) with target-specific oligonucleotides were used to measure miRNA targets expression levels. The manufacturer's protocol was followed for both styles of RT-qPCR. The qPCR reactions were performed on a QuantStudio3 (Thermo Fisher Scientific) Real-Time PCR system. Each RT-qPCR reaction was done using three biological replicates from independent RNA samples. Relative changes in miRNA or target expression levels were determined by the ΔΔCt method using small nucleolar RNA sn2841 for miRNA level normalization, or Alpha Tubulin (*tba-1*) for target expression normalization. TaqMan miRNA probes IDs and target oligonucleotide sequences are listed in Supplementary Data 2.

miRNA cloning, sequencing, and analysis

Total RNA was extracted from either young adult worm pellets using TRI Reagent (Sigma-Aldrich) and resuspended in 20 μL sterile, RNase-free water. Small RNA cloning was performed with the NEBNext multiplex small RNA library kit and according to the manufacturer's protocol. Hiseq 4000 SR50 sequencing reads were mapped to the genome and cDNA using custom PERL (5.10.1) scripts and Bowtie 0.12.7[62]. Databases used include *C. elegans* genome (WormBase release WS215), Repbase 15.10[63], and miRBase 16[64]. The samples were normalized to the total gene expression (geex) reads excluding structural RNA (struc) and transformed in reads per million (RPM). The mean $\log_2$ value of three biological replicates for every condition was used to generate graphs. Processed miRNA sequencing data are listed in Supplementary Data 5.

Western blotting

Extracts were quantified with Bio-Rad Protein Assay and equal amounts of proteins were mixed in 4X SDS loading buffer before being boiled at 99 °C for 10 min. Samples were resolved onto an 8% polyacrylamide gel and transferred to 0.45 μm nitrocellulose blotting membranes (GE Healthcare). Membranes were incubated overnight at 4 °C with the primary antibodies rabbit anti-ALG-1/2 (1:1000), rabbit anti-ALG-1 (1:1000), rabbit anti-HA (1:5000) (NEB C29F4), mouse anti-V5 tag (1:500) (Abcam ab27671), mouse anti-FLAG M2 (1:5000) (Sigma-Aldrich F1804) and mouse anti β-actin (1:10,000). Membranes were then incubated with secondary antibody Sheep Anti-Mouse IgG (1:10,000) or Goat Anti-Rabbit IgG (1:5000). Imaging was done using a ChemiDoc MP imaging system (BioRad) and images were processed with Image Lab software.

Specific miRISC purification: 2′-O-methyl pulldown

Specific biotinylated miRNA probes and an unrelated control were used with 2 mg of protein extract for each genotype assessed and the miRISC was pulled down as described in Jannot et al. [44]. Briefly, a 2 mg protein sample is precleared with an unrelated probe bound to Dynabeads M-280 streptavidin beads (Life Technologies 11205D) for 45 min at room temperature. The protein sample is then split in half and is either incubated with an unrelated probe, or a let-7 or miR-77 complementary probe bound to Dynabeads M-280 streptavidin beads for 45 min at room temperature. Beads are then washed twice with lysis buffer (100 mM Potassium Acetate, 30 mM Hepes-Potassium Hydroxide pH 7.4, 2 mM Magnesium Acetate, 1 mM DTT, 0.5% [v/v] triton, 2% [v/v] RNase inhibitors and protease inhibitors). Beads are finally resuspended in SDS loading buffer (10 mM Tris-HCl [pH 6.8], 2% [w/v] SDS, 100 mM DTT, and 10% [v/v] glycerol) and boiled at 99 °C for 10 min before gel loading. Probe sequences are listed in Supplementary Data 2.

C. elegans alg-2 RNAi

E. coli HT115 bacteria transformed with L4440 plasmid expressing a portion of *alg-2* gene sequence double-stranded RNA under IPTG-inducible T7 promoters were seeded on NGM plates containing IPTG. The plates were activated overnight at 25 °C. L4 worms of the specified genotypes were placed on either *alg-2* or control RNAi plates at 25 °C for 24 h before being removed. Embryonic lethality was scored 48 h post RNAi-fed worms were removed.

N-terminomics/Terminal Isotopic Labeling of Substrates (TAILS) and shotgun proteomics

Total worm extracts of WT and *dpf-3(xe68)* worms were treated with 6 M guanidine HCl (pH 8.0) and subjected to a N-terminomics/TAILS and shotgun proteomics workflow. Samples were reduced with 5 mM DTT (Gold Biotechnology) at 37 °C for 1 h and alkylated with 15 mM IAA (GE Healthcare) in the dark at room temperature for 30 min followed by quenching with 15 mM DTT. The pH was adjusted to 6.5 before the samples were isotopically labeled with a final concentration of 40 mM deuterated heavy formaldehyde (*dpf-3(xe68)* samples) and control samples (WT samples) with 40 mM light formaldehyde in presence of 40 mM sodium cyanoborohydride overnight at 37 °C. Next, samples were combined and were precipitated using acetone/methanol (8:1). The resulting pellet was resuspended in 1 M NaOH and the proteins were subjected to trypsin (Promega) digestion overnight at 37 °C. For pre-enrichment TAILS (pre-TAILS)/shotgun proteomics, 10% of the trypsin digested samples were collected and the pH was adjusted to 3 with 100% formic acid. The rest of the samples were adjusted to a pH of 6.5 and incubated with a 3-fold excess (w/w) of dendritic polyglycerol aldehyde polymer overnight at 37 °C. Unbound peptides from the polymer-bound peptides were filtered out by centrifugal filter unit with 10-kDa cut-off membrane (Amicon Ultra, Millipore) at 10,000 g for 5 min. The flow-through was collected and the Amicon columns were washed with 100 mM Tris-HCl, pH 6.5. The pH of the samples was adjusted to 3 with 100% Formic acid. Both pre-TAILS and TAILS samples were then desalted using Sep-Pak C18 columns and lyophilized before submitting for LC-MS/MS analysis to the Southern Alberta Mass Spectrometry core facility, University of Calgary, Canada.

TAILS samples HPLC and mass spectrometry

All liquid chromatography and mass spectrometry associated to TAILS experiments were carried out by the Southern Alberta Mass Spectrometry core facility at the University of Calgary, Canada. Analysis was performed on an Orbitrap Fusion Lumos Tribrid mass spectrometer (Thermo Fisher Scientific) operated with Xcalibur (version 4.0.21.10) and coupled to a Thermo Scientific Easy-nLC (nanoflow Liquid Chromatography) 1200 system. Tryptic peptides (2 µg) were loaded onto a C18 trap (75 µm × 2 cm; Acclaim PepMap 100, P/N 164946; Thermo Fisher Scientific) at a flow rate of 2 µL/min of solvent A (0.1% formic acid and 3% acetonitrile in LC-mass spectrometry grade water). Peptides were eluted using a 120 min gradient from 5 to 40% (5% to 28% in 105 min followed by an increase to 40% B in 15 min) of solvent B (0.1% formic acid in 80% LC-mass spectrometry grade acetonitrile) at a flow rate of 0.3% µL/min and separated on a C18 analytical column (75 µm × 50 cm; PepMap RSLC C18; P/N ES803; Thermo Fisher Scientific). Peptides were then eletrosprayed using 2.3 kV into the ion transfer tube (300 °C) of the Orbitrap Lumos operating in positive mode. The Orbitrap first performed a full mass spectrometry scan at a resolution of 120,000 FWHM to detect the precursor ion having a mass-to-charge ratio (m/z) between 375 and 1575 and a + 2 to +4 charge. The Orbitrap AGC (Auto Gain Control) and the maximum injection time were set at 4 × 105 and 50 ms, respectively. The Orbitrap was operated using the top speed mode with a 3 s cycle time for precursor selection. The most intense precursor ions presenting a peptidic isotopic profile and having an intensity threshold of at least 2 × 104 were isolated using the quadrupole (isolation window of m/z 0.7) and fragmented with HCD (38% collision energy) in the ion routing Multipole. The fragment ions (MS2) were analyzed in the Orbitrap at a resolution of 15,000. The AGC, the maximum injection time and the first mass were set at 1 × 105, 105 ms, and 100 ms, respectively. Dynamic exclusion was enabled for 45 s to avoid of the acquisition of the same precursor ion having a similar m/z (±10 ppm).

TAILS proteomic data and bioinformatic analysis

Spectral data were matched to peptide sequences from the *C. elegans* UniProt protein database using the MaxQuant software package v.1.6.0.1, peptide-spectrum match false discovery rate (FDR) of <0.01 for the shotgun proteomics data and <0.05 for the N-terminomics/TAILS data. Search parameters included a mass tolerance of 20 p.p.m. for the parent ion, 0.05 Da for the fragment ion, carbamidomethylation of cysteine residues (+57.021464), variable N-terminal modification by acetylation (+42.010565 Da), and variable methionine oxidation (+15.994915 Da). For the shotgun proteomics data, cleavage site specificity was set to Trypsin/P (search for free N-terminus and only for lysines), with up to two missed cleavages allowed. The files evidence.txt and proteinGroups.txt were analyzed by MaxQuant[65]. For the N-terminomics/TAILS data, the cleavage site specificity was set to semi-ArgC (search for free N-terminus) for the TAILS data and was set to ArgC for the preTAILS data, with up to two missed cleavages allowed. Significant outlier cut-off values were determined after log(2) transformation by boxplot-and-whiskers analysis using the BoxPlotR tool. Database searches were limited to a maximal length of 40 residues per peptide. Peptide sequences matching reverse or contaminant entries were removed. Raw peptide data are listed in Supplementary Data 3.

In vitro cleaving assay

DPF-3 protein was purified by immunoprecipitation using Anti-FLAG M2 Magnetic Beads (Sigma-Aldrich). 800 µg of protein extract of either *dpf-3::flag-ha* or *dpf-3(S784A)::flag-ha* worms were incubated for 2 h at 4 °C with 20 µL of previously twice washed beads with TBS (50 mM Tris-HCl, 150 mM NaCl) in a total volume of 500 µL. The DPF-3 bound beads were then washed 3 times with TBS and 5% of the beads were kept for western blotting to verify the efficiency of the purification. The remaining beads were incubated with 100 µL of resuspended custom-made peptide (in TBS supplemented with 2 mM TCEP) mimicking ALG-2 N-terminal at a 0.1 nM/µL concentration. Aliquots of the peptide were taken at 0 min, 30 min, 60 min, 120 min and 240 min, and put into a buffer to stop the reaction (2% acetonitrile, 0.1% trifluoroacetic acid, 2 mM TCEP) The samples were kept at −80 °C until peptide preparation for mass spectrometry analysis.

In vitro cleaving assay peptide preparation and mass spectrometry

Peptide purification and mass spectrometry analyses were performed by the Proteomics Platform of the CHU de Québec Research Center (Québec, Qc, Canada). 94 ng of peptides were purified on StageTips using C18 Empore solid phase[66] and vacuum dried. Samples were resuspended in 2% acetonitrile (ACN), 0.05% trifluoroacetic acid (TFA) to inject 20 pmol in LC-MS/MS. Prior to injection, 8 fmol of Cytochrome C digest (Thermo Scientific) was added to the samples in order to control the stability of the signal. Samples were analyzed by nanoLC-MS/MS using a Dionex UltiMate 3000 nanoRSLC chromatography system (Thermo Fisher Scientific) connected to an Orbitrap Fusion mass spectrometer (Thermo Fisher Scientific) equipped with a nanoelectrospray ion source. Peptides were trapped at 20 µl/min in loading solvent (2% ACN, 0.05% TFA) on a 5 mm × 300 µm C18 pepmap cartridge (Thermo Fisher Scientific) for 5 min. Then, the pre-column was switched online with a 50 cm × 75 µm internal diameter separation column (Pepmap Acclaim column, ThermoFisher Scientific) and the peptides were eluted with a linear gradient from 5–40% solvent B (A: 0.1% FA, B: 80% ACN, 0.1% FA) in 30 min, at 300 nL/min (60 min total runtime). Mass spectra were acquired using a parallel reaction monitoring acquisition mode using Thermo XCalibur software version 4.1.50. Targeted MS2 scans were acquired in the Orbitrap at a resolution of 30,000 using 0.7 m/z quadruple precursor isolation windows and fragmentation by Higher energy Collision-induced Dissociation (HCD) with 35% of collision energy. Each peptide was monitored through 4 precursors corresponding charge stage +2 to +5 (Supplementary Data 4).

In vitro cleaving assay mass spectrometry data analysis

RAW files were imported in Skyline software[67]. For each precursor, extracted ion chromatogram from the 6 most intense ions were used for peak integration. After manual inspection of the peaks, the resulting the total areas from the 2+ peptides were exported into Microsoft Excel for data analysis.

Generation of CRISPR-Cas9 mutant *C. elegans* strains

Guide RNAs were designed using the CHOPCHOP web platform (https://chopchop.cbu.uib.no/)[68]. Repair templates were designed according to Paix et al. [69] guidelines. Reconstituted Cas9 RNP complex mix (injection mix) was prepared as follows: 1.25–2.50 µg Cas9 (Alt-R® *S.p.* Cas9) Nuclease V3 (ID Technology), 0.3 µg guide RNA (gene of interest and roller injection co-marker), 1.625 µM repair template (gene of interest and roller injection co-marker), 6.7 µg tracrRNA, 25 mM KCl, 7.5 mM HEPES, all diluted in 20 µL total volume of RNase-free H_2O. Injection needles were made from glass capillaries (Tritech Research Inc.) pulled by a flaming micropipette puller (Sutter Instrument Co., Model P-97), and the sharp end was cleared open using hydrofluoric acid. The needle was filled with the injection mix and mounted on a moveable arm attached to a Nikon Eclipse TE2000-U inverted bright-field microscope. Young adult and adult Bristol N2 worms were selected for injection and placed under the microscope. The mounted injection needle was brought to the gonad using the moveable arm and precisely penetrated the gonad as viewed under the microscope. The injection mix was unloaded into the gonad using a pressurized air system connected to the needle blunt end. Injected worms' progeny was then screened for roller phenotype (injection marker) and roller worms were genotyped by PCR for mutation of interest. Guide and repair template sequences are listed in Supplementary Data 2.

Statistical analysis

Data are displayed as mean ± SD. Statistical significance between conditions was performed using Graphpad Prism 10 software with two-sided Fisher's exact test, two-tailed Mann-Whitney's test (when samples distribution failed normality test), two-tailed Student's t-test (two-tailed one-sample t-tests were used for quantification of western blots with a theoretical mean of 1.0) or two-way ANOVA depending on the dataset. ALG-1 and ALG-2 mass spectrometry data were analyzed using either two-tailed Student t-test or limma-eBayes method (two-sided) with Benjamini-Hochberg multiple testing corrections. Results were considered as statistically significant when $p < 0.05$.

Reporting summary

Further information on research design is available in the Nature Portfolio Reporting Summary linked to this article.

Data availability

The microRNA sequencing data generated in this study have been deposited in NCBI Gene Expression Omnibus (https://www.ncbi.nlm.nih.gov/geo/) under accession code GSE276186. ALG-1 and ALG-2 immunoprecipitation and mass spectrometry analysis data generated in this study have been deposited to the ProteomeXchange Consortium via the PRIDE partner repository (https://www.ebi.ac.uk/pride/) under accession code PXD060454. TAILS experiments data generated in this study have been deposited to the ProteomeXchange Consortium via the PRIDE partner repository (https://www.ebi.ac.uk/pride/) under accession code PXD055867. Source data are provided with this paper.

Code availability

This study did not use or create a custom code to generate any data supporting the findings in the study.

References

1. Bartel, D. P. Metazoan microRNAs. *Cell* **173**, 20–51 (2018).
2. Liu, J. et al. A role for the P-body component GW182 in microRNA function. *Nat. Cell Biol.* **7**, 1261–1266 (2005).
3. Rehwinkel, J., Behm-Ansmant, I., Gatfield, D. & Izaurralde, E. A crucial role for GW182 and the DCP1:DCP2 decapping complex in miRNA-mediated gene silencing. *RNA* **11**, 1640–1647 (2005).
4. Eulalio, A., Huntzinger, E. & Izaurralde, E. GW182 interaction with Argonaute is essential for miRNA-mediated translational repression and mRNA decay. *Nat. Struct. Mol. Biol.* **15**, 346–353 (2008).
5. Bartel, D. P. MicroRNAs: genomics, biogenesis, mechanism, and function. *Cell* **116**, 281–297 (2004).
6. Frédérick, P. M. & Simard, M. J. Regulation and different functions of the animal microRNA-induced silencing complex. *Wiley Interdiscip. Rev. RNA* **13**, e1701 (2022).
7. Jonas, S. & Izaurralde, E. Towards a molecular understanding of microRNA-mediated gene silencing. *Nat. Rev. Genet.* **16**, 421–433 (2015).
8. Vasudevan, S., Tong, Y. & Steitz, J. A. Switching from repression to activation: MicroRNAs can up-regulate translation. *Science* **318**, 1931–1934 (2007).
9. Fukaya, T. & Tomari, Y. MicroRNAs mediate gene silencing via multiple different pathways in drosophila. *Mol. Cell* **48**, 825–836 (2012).
10. Jannot, G. et al. GW182-free microRNA silencing complex controls post-transcriptional gene expression during *Caenorhabditis elegans* embryogenesis. *PLoS Genet.* **12**, e1006484 (2016).
11. Dallaire, A., Frédérick, P. M. & Simard, M. J. Somatic and germline MicroRNAs form distinct silencing complexes to regulate their target mRNAs differently. *Dev. Cell* **47**, 239–247.e4 (2018).
12. Hutvagner, G. & Simard, M. J. Argonaute proteins: key players in RNA silencing. *Nat. Rev. Mol. Cell Biol.* **9**, 22–32 (2008).
13. Song, J. J., Smith, S. K., Hannon, G. J. & Joshua-Tor, L. Crystal structure of Argonaute and its implications for RISC slicer activity. *Science* **305**, 1434–1437 (2004).
14. Yamaguchi, S. et al. Crystal structure of *Drosophila* Piwi. *Nat. Commun.* **11**, 858 (2020).
15. Schirle, N. T. & MacRae, I. J. The crystal structure of human Argonaute2. *Science* **336**, 1037–1040 (2012).
16. Vasquez-Rifo, A. et al. Developmental characterization of the microRNA-specific *C. elegans* Argonautes *alg-1* and *alg-2*. *PLoS ONE* **7**, e33750 (2012).
17. Seroussi, U. et al. A comprehensive survey of *C. elegans* argonaute proteins reveals organism-wide gene regulatory networks and functions. *Elife* **12**, e83853 (2023).
18. Grishok, A. et al. Genes and mechanisms related to RNA interference regulate expression of the small temporal RNAs that control *C. elegans* developmental timing. *Cell* **106**, 23–34 (2001).
19. Tops, B. B. J., Plasterk, R. H. A. & Ketting, R. F. The *Caenorhabditis elegans* Argonautes ALG-1 and ALG-2: almost identical yet different. *Cold Spring Harb. Symp. Quant. Biol.* **71**, 189–194 (2006).
20. Aalto, A. P. et al. Opposing roles of microRNA Argonautes during *Caenorhabditis elegans* aging. *PLoS Genet.* **14**, e1007379 (2018).
21. Sasaki, T., Shiohama, A., Minoshima, S. & Shimizu, N. Identification of eight members of the Argonaute family in the human genome. *Genomics* **82**, 323–330 (2003).
22. Hafner, M. et al. Transcriptome-wide identification of RNA-binding protein and microRNA target sites by PAR-CLIP. *Cell* **141**, 129–141 (2010).
23. Hu, Q. et al. DICER- and AGO3-dependent generation of retinoic acid–induced DR2 Alu RNAs regulates human stem cell proliferation. *Nat. Struct. Mol. Biol.* **19**, 1168–1175 (2012).
24. Adiliaghdam, F. et al. A Requirement for Argonaute 4 in mammalian antiviral defense. *Cell Rep.* **30**, 1690–1701.e4 (2020).
25. Liu, J. et al. Argonaute2 is the catalytic engine of mammalian RNAi. *Science* **305**, 1437–1441 (2004).
26. Meister, G. et al. Human Argonaute2 mediates RNA cleavage targeted by miRNAs and siRNAs. *Mol. Cell* **15**, 185–197 (2004).
27. Nakanishi, K. Anatomy of four human Argonaute proteins. *Nucleic Acids Res* **50**, 6618–6638 (2022).
28. Ding, L., Spencer, A., Morita, K. & Han, M. The developmental timing regulator AIN-1 interacts with miRISCs and may target the Argonaute protein ALG-1 to cytoplasmic P bodies in *C. elegans*. *Mol. Cell* **19**, 437–447 (2005).
29. Zhang, L. et al. Systematic identification of *C. elegans* miRISC proteins, miRNAs, and mRNA targets by their Interactions with GW182 proteins AIN-1 and AIN-2. *Mol. Cell* **28**, 598–613 (2007).
30. Zhang, H., Chen, Y., Keane, F. M. & Gorrell, M. D. Advances in understanding the expression and function of dipeptidyl peptidase 8 and 9. *Mol. Cancer Res.* **11**, 1487–1496 (2013).
31. Geiss-Friedlander, R. et al. The cytoplasmic peptidase DPP9 is rate-limiting for degradation of proline-containing peptides. *J. Biol. Chem.* **284**, 27211–27219 (2009).
32. Zhang, H. et al. Identification of novel dipeptidyl peptidase 9 substrates by two-dimensional differential in-gel electrophoresis. *FEBS J.* **282**, 3737–3757 (2015).
33. Gudipati, R. K. et al. Deep quantification of substrate turnover defines protease subsite cooperativity. *Mol. Syst. Biol.* **20**, 1303–1328 (2024).
34. Gudipati, R. K. et al. Protease-mediated processing of Argonaute proteins controls small RNA association. *Mol. Cell* **81**, 2388–2402.e8 (2021).
35. Sulston, J. E. & Horvitz, H. R. Post-embryonic cell lineages of the nematode, *Caenorhabditis elegans*. *Dev. Biol.* **56**, 110–156 (1977).
36. Shah, V. N. et al. Casein kinase 1 and 2 phosphorylate Argonaute proteins to regulate miRNA-mediated gene silencing. *EMBO Rep.* **24**, e57250 (2023).
37. Quévillon Huberdeau, M. et al. A specific type of Argonaute phosphorylation regulates binding to microRNAs during *C. elegans* development. *Cell Rep.* **41**, 111822 (2022).

38. Singh, R. N. & Sulston, J. E. Some observations on moulting in *Caenorhabditis elegans*. *Nematologica* **24**, 63–71 (1978).
39. Reinhart, B. J. et al. The 21-nucleotide let-7 RNA regulates developmental timing in *Caenorhabditis elegans*. *Nature* **403**, 901–906 (2000).
40. Zinovyeva, A. Y., Bouasker, S., Simard, M. J., Hammell, C. M. & Ambros, V. Mutations in conserved residues of the *C. elegans* microRNA Argonaute ALG-1 identify separable functions in ALG-1 miRISC loading and target repression. *PLoS Genet.* **10**, e1004286 (2014).
41. Lin, S. Y. et al. The *C elegans* hunchback homolog, *hbl-1*, controls temporal patterning and is a probable microRNA target. *Dev. Cell* **4**, 639–650 (2003).
42. Großhans, H., Johnson, T., Reinert, K. L., Gerstein, M. & Slack, F. J. The temporal patterning microRNA let-7 regulates several transcription factors at the larval to adult transition in *C. elegans*. *Dev. Cell* **8**, 321–330 (2005).
43. Abrahante, J. E. et al. The Caenorhabditis elegans hunchback-like gene lin-57/hbl-1 controls developmental time and is regulated by microRNAs. *Dev. Cell* **4**, 625–637 (2003).
44. Jannot, G., Vasquez-Rifo, A. & Simard, M. J. Argonaute pull-down and RISC analysis using 2′-*O*-methylated oligonucleotides affinity matrices. *Methods Mol. Biol.* **725**, 233–249 (2011).
45. Kleifeld, O. et al. Isotopic labeling of terminal amines in complex samples identifies protein N-termini and protease cleavage products. *Nat. Biotechnol.* **28**, 281–288 (2010).
46. Wang, L., Main, K., Wang, H., Julien, O. & Dufour, A. Biochemical tools for tracking proteolysis. *J. Proteome Res.* **20**, 5264–5279 (2021).
47. Anowai, A., Chopra, S., Mainoli, B., Young, D. & Dufour, A. N-terminomics/TAILS of tissue and liquid biopsies. *Methods Mol. Biol.* **2456**, 85–94 (2022).
48. Sharif, H. et al. Dipeptidyl peptidase 9 sets a threshold for CARD8 inflammasome formation by sequestering its active C-terminal fragment. *Immunity* **54**, 1392–1404.e10 (2021).
49. Hollingsworth, L. R. et al. DPP9 sequesters the C terminus of NLRP1 to repress inflammasome activation. *Nature* **592**, 778–783 (2021).
50. Varadi, M. et al. AlphaFold protein structure database in 2024: providing structure coverage for over 214 million protein sequences. *Nucleic Acids Res.* **52**, D368–D375 (2024).
51. Hoogewijs, D., Houthoofd, K., Matthijssens, F., Vandesompele, J. & Vanfleteren, J. R. Selection and validation of a set of reliable reference genes for quantitative *sod* gene expression analysis in *C. elegans*. *BMC Mol. Biol.* **9**, 1–8 (2008).
52. Bressendorff, S. et al. The N-coil and the globular N-terminal domain of plant ARGONAUTE1 are interaction hubs for regulatory factors. *Biochem J.* **480**, 957–974 (2023).
53. Bressendorff, S. et al. Importance of an N-terminal structural switch in the distinction between small RNA-bound and free ARGONAUTE. *Nat. Struct. Mol. Biol.* https://doi.org/10.1038/S41594-024-01446-9 (2025).
54. Jannot, G. et al. The ribosomal protein RACK1 is required for microRNA function in both *C. elegans* and humans. *EMBO Rep.* **12**, 581–586 (2011).
55. Frédérick, P.-M., Jannot, G., Banville, I. & Simard, M. J. Interaction between a J-domain co-chaperone and a specific Argonaute protein contributes to microRNA function in animals. *Nucleic Acids Res.* **52**, 6253–6268 (2024).
56. Su, H., Trombly, M. I., Chen, J. & Wang, X. Essential and overlapping functions for mammalian Argonautes in microRNA silencing. *Genes Dev.* **23**, 304–317 (2009).
57. Brosnan, C. A., Palmer, A. J. & Zuryn, S. Cell-type-specific profiling of loaded miRNAs from *Caenorhabditis elegans* reveals spatial and temporal flexibility in Argonaute loading. *Nat. Commun.* **12**, 2194 (2021).
58. Duan, Y. et al. Modeling neurodevelopmental disorder-associated human AGO1 mutations in *Caenorhabditis elegans* Argonaute alg-1. *Proc. Natl. Acad. Sci. USA* **121**, e2308255121 (2024).
59. Brown, K. C., Svendsen, J. M., Tucci, R. M., Montgomery, B. E. & Montgomery, T. A. ALG-5 is a miRNA-associated Argonaute required for proper developmental timing in the *Caenorhabditis elegans* germline. *Nucleic Acids Res.* **45**, 9093–9107 (2017).
60. Heß, L. et al. Dipeptidyl-peptidase 9 regulates the dynamics of tumorigenesis and metastasis in breast cancer. *Biochim Biophys. Acta Mol. Basis Dis.* **1870**, 16733 (2024).
61. Brenner, S. The genetics of *Caenorhabditis elegans*. *Genetics* **77**, 71–94 (1974).
62. Langmead, B., Trapnell, C., Pop, M. & Salzberg, S. L. Ultrafast and memory-efficient alignment of short DNA sequences to the human genome. *Genome Biol.* **10**, R25 (2009).
63. Jurka, J. et al. Repbase update, a database of eukaryotic repetitive elements. *Cytogenet. Genome Res.* **110**, 462–467 (2005).
64. Kozomara, A. & Griffiths-Jones, S. miRBase: integrating microRNA annotation and deep-sequencing data. *Nucleic Acids Res.* **39**, D152–D157 (2011).
65. Cox, J. & Mann, M. MaxQuant enables high peptide identification rates, individualized p.p.b.-range mass accuracies and proteome-wide protein quantification. *Nat. Biotechnol.* **26**, 1367–1372 (2008).
66. Rappsilber, J., Ishihama, Y. & Mann, M. Stop and go extraction tips for matrix-assisted laser desorption/ionization, nanoelectrospray, and LC/MS sample pretreatment in proteomics. *Anal. Chem.* **75**, 663–670 (2003).
67. Pino, L. K. et al. The Skyline ecosystem: Informatics for quantitative mass spectrometry proteomics. *Mass Spectrom. Rev.* **39**, 229–244 (2020).
68. Labun, K. et al. CHOPCHOP v3: expanding the CRISPR web toolbox beyond genome editing. *Nucleic Acids Res.* **47**, W171–W174 (2019).
69. Paix, A., Folkmann, A. & Seydoux, G. Precision genome editing using CRISPR-Cas9 and linear repair templates in *C. elegans*. *Methods* **121–122**, 86–93 (2017).

Acknowledgements

We thank Lamia Samri for her technical help; the CRCHU de Québec - Université Laval Genomics and Proteomics Center for their help with the miRNA sequencing and the in vitro cleavage assays; Daniel Hess for performing the mass spectrometry of ALG-1, DPF-3, and ALG-2 immunoprecipitations; Jan Seebacher and A. Alexander Smith for support in mass spectrometry data analysis; and members of the Simard laboratory for helpful discussions and feedback on the manuscript. Some strains were provided by the *Caenorhabditis* Genetics Center (CGC), which is funded by NIH Office of Research Infrastructure Programs (P40 OD010440). The project was supported through funding by the Fonds de Recherche en Santé du Québec and the Natural Sciences and Engineering Research Council of Canada (to L-M.H. and P-M.F.); the National Science Center (NCN), Poland, SONATA BIS 2021/42/E/NZ1/00336 and OPUS 2022/45/B/NZ2/02183 (to R.K.G); an NSERC Discovery Grant (DGECR-2019-00112), Alberta Innovates AICE concepts (202102341) and Canadian Institutes of Health Research (449589) (to A.D.); the NCCR RNA and Disease, a National Center of Excellence in Research, funded by the Swiss National Science (grant numbers 182880 & 205601) and the Novartis Research Foundation through the Friedrich Miescher Institute for Biomedical Research (to H.G.); and the Natural Sciences and Engineering Research Council of Canada and Canadian Institutes of Health Research (to M.J.S.).

Author contributions

L-M.H.: Conceptualization, investigation, formal analysis, writing—original draft, reviewing and editing. P-M.F.: Conceptualization, investigation, writing—original draft, reviewing and editing. R.K.G.: Conceptualization, investigation, writing—original draft, reviewing and

editing. P.M.: Conceptualization, investigation. F.H., C.D., and S.L.: Investigation. D.Y.: investigation and formal analysis of the TAILS experiments. A.D.: Conceptualization, investigation, and formal analysis of the TAILS experiments, writing—original draft, reviewing and editing, funding acquisition. H.G.: Conceptualization, writing—original draft, reviewing and editing, supervision, funding acquisition. M.J.S.: Conceptualization, investigation, formal analysis, writing—original draft, reviewing and editing, supervision, funding acquisition.

Competing interests

The authors declare no competing interests.

Additional information

Supplementary information The online version contains supplementary material available at https://doi.org/10.1038/s41467-025-58141-6.

Correspondence and requests for materials should be addressed to Martin J. Simard.

Peer review information *Nature Communications* thanks the anonymous reviewer(s) for their contribution to the peer review of this work. A peer review file is available.

Reprints and permissions information is available at http://www.nature.com/reprints

Publisher's note Springer Nature remains neutral with regard to jurisdictional claims in published maps and institutional affiliations.

Open Access This article is licensed under a Creative Commons Attribution-NonCommercial-NoDerivatives 4.0 International License, which permits any non-commercial use, sharing, distribution and reproduction in any medium or format, as long as you give appropriate credit to the original author(s) and the source, provide a link to the Creative Commons licence, and indicate if you modified the licensed material. You do not have permission under this licence to share adapted material derived from this article or parts of it. The images or other third party material in this article are included in the article's Creative Commons licence, unless indicated otherwise in a credit line to the material. If material is not included in the article's Creative Commons licence and your intended use is not permitted by statutory regulation or exceeds the permitted use, you will need to obtain permission directly from the copyright holder. To view a copy of this licence, visit http://creativecommons.org/licenses/by-nc-nd/4.0/.

© The Author(s) 2025